JGR Oceans

RESEARCH ARTICLE
10.1029/2020JC016193

Year-Round Measurements of the Irminger Current: Variability of a Two-Core Current System Observed in 2014–2016

M. F. de Jong[1], L. de Steur[2], N. Fried[1], R. Bol[1], and S. Kritsotalakis[3]

[1]Royal Netherlands Institute for Sea Research and Utrecht University, Texel, Netherlands, [2]Norwegian Polar Institute, Tromsø, Norway, [3]Alfred Wegener Institute, Bremerhaven, Germany

Key Points:
- First year-round observations of the two-core Irminger Current over the Reykjanes Ridge show a mean transport of 10.6 ± 1.4 Sv (st error)
- IC transports are highly variable with a std of 9.2 Sv (daily values) and 4.4 Sv (monthly values); the western core is the most variable
- Mixing to densities near 27.7 kg m^{-3} occurred over the array in both winters (deepest in the west), contributing to the overturning

Supporting Information:
- Supporting Information S1

Correspondence to:
M. F. de Jong,
femke.de.jong@nioz.nl

Citation:
de Jong, M. F., de Steur, L., Fried, N., Bol, R., & Kritsotalakis, S. (2020). Year-round measurements of the Irminger Current: Variability of a two-core current system observed in 2014–2016. *Journal of Geophysical Research: Oceans*, *125*, e2020JC016193. https://doi.org/10.1029/2020JC016193

Received 27 FEB 2020
Accepted 22 SEP 2020
Accepted article online 29 SEP 2020

Abstract The Irminger Current (IC), flowing northeastward along the western flank of the Reykjanes Ridge, is an important component in the overturning of the North Atlantic subpolar gyre. A 2-year (2014–2016) time series from moored observations shows that the IC consists of two highly variable current cores. A subsampling experiment, using an ocean reanalysis, showed that this current's variability is adequately captured by the array. The two current cores contribute nearly equally to the mean volume transport. The total 2-year mean transport was found to be 10.6 Sv with a standard deviation of daily (monthly) values of 9.2 Sv (4.4 Sv) and a standard error of 1.4 Sv. Mean heat and freshwater transport were 0.21 PW and −22.5 mSv, respectively ($S_{ref} = 34.92$). The volume transport is strongest in spring, and the average over the first year (8.6 Sv) was lower than that of the second year (12.4 Sv), coinciding with an increase in the density gradient over the array in the second year. The variability of the total transport is dominated by variations in the western core, while the warmer, saltier eastern core contributes more to the heat and (negative) freshwater transport. During the two observed winters, which were marked by exceptional deep convection in the central Irminger Sea, mixed layer deepening down to 400 m depth and outcropping of the 27.7 kg m^3 isopycnal were observed within the IC.

Plain Language Summary The Irminger Current flows northeastward along the Reykjanes Ridge in the Irminger Sea. It transports warm saline water originating from the North Atlantic Current in the upper layers and deep waters coming from the overflows on the Iceland-Scotland Ridge. This paper describes the first year-round moored observations of velocity, temperature, and salinity of this current system. These new observations show that the Irminger Current consists of two cores that contribute equally to the mean transport. The core closer to the top of the ridge is more stable and transports warmer, more saline water, while the core closer to the center of the Irminger Basin is more variable in location and transport. During the observed winters, strong atmospheric cooling created deep mixed layers down to 400 m at the mooring locations. This observed cooling and densification of the upper ocean waters indicate that this current system is an important contributor to the overturning in the Northeastern Atlantic.

1. Introduction

The Atlantic Meridional Overturning Circulation (AMOC) in the subpolar North Atlantic consists of a multitude of smaller currents that transport buoyant water northward and denser water southward. The Overturning in the Subpolar North Atlantic Program (OSNAP; Lozier et al., 2017, 2019) array was designed to measure the total overturning in the subpolar gyre. The Irminger Current (IC), which is part of the cyclonic Subpolar Gyre circulation, transports warm, salty water northward along the western flank of the Reykjanes Ridge (RR) in the Irminger Sea (Figure 1). In the upper layers, this current is composed by Irminger Subpolar Mode Water (SPMW; García-Ibáñez et al., 2015). This SPMW is relatively warm and saline due to its origin from the North Atlantic Current (Brambilla & Talley, 2008). Progressively denser SPMW flows south in the East RR Current (Orvik & Niiler, 2002) and enters the Irminger Sea across the RR (Petit et al., 2019). The Irminger SPMW over the RR is denser than any of the SPMW cores found further east (Brambilla & Talley, 2008; de Boisséson et al., 2012; García-Ibáñez et al., 2015). This, still relatively warm, IC water travels cyclonically around the Irminger Sea (Krauss, 1995; Reverdin et al., 2003) and is found just off the East Greenland shelf as part of the East Greenland Current and continues after Cape Farewell as part of

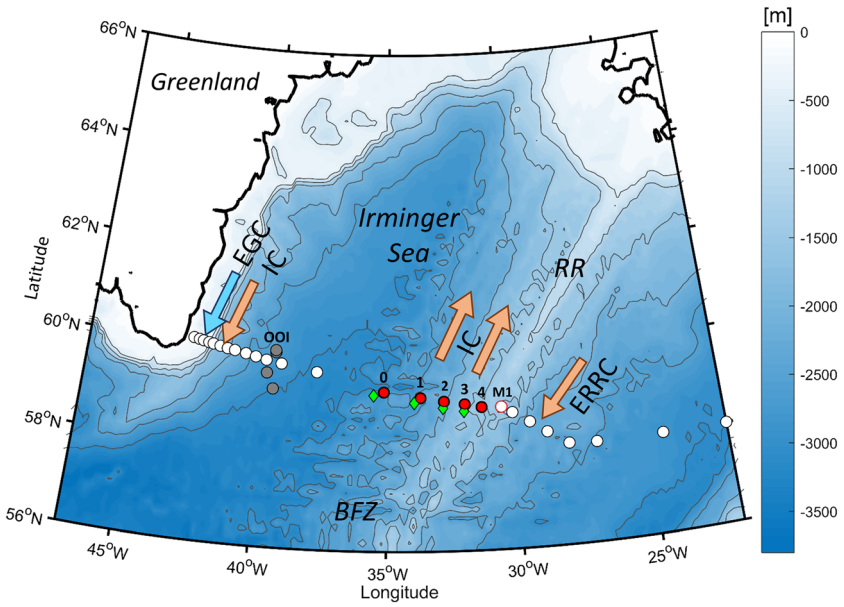

Figure 1. Mooring locations and schematic diagram of currents in the Irminger Sea. Indicated currents are the Irminger Current (IC, consisting of two cores), the East Greenland Current (EGC), and the East Reykjanes Ridge Current (ERRC). Topographic features indicated are the Reykjanes Ridge (RR) and the Bight Fracture Zone (BFZ). The IC array is indicated with red dots, while the other OSNAP moorings are indicated with white dots. The US mooring M1 (red rimmed white circle) neighboring the IC moorings on the RR is included in the analysis here. Green diamonds are locations of the LOCO array that was deployed in 2003–2004. Gray dots are OOI moorings in the central Irminger Sea.

the West Greenland Current (Cuny et al., 2002; de Jong et al., 2014). There, it is typically referred to as Irminger Water.

The deeper waters underneath the SPMW consist of North East Atlantic Deep Water (NEADW; van Aken & Becker, 1996), which originates from Iceland Scotland Overflow Water (ISOW). ISOW enters the eastern Atlantic through the Faroe Bank Channel and over the Iceland Faroe Ridge (van Aken & de Boer, 1995) and then enters the western Atlantic through the Charlie Gibbs Fracture Zone (Bower et al., 2002), Bight Fracture Zone (Petit et al., 2018), and other smaller fractures zones along the ridge. Along the way, the ISOW is substantially modified through entrainment over overlying waters (Dickson et al., 2002; Racapé et al., 2019; Yashayaev, 2007). The resulting water mass in the Irminger Sea, NEADW, is less saline and less dense and, unlike the ISOW east of the RR, does not exhibit a clear core with a density gradient steepening toward the bottom. Nevertheless, the NEADW continues cyclonically around the boundary of the Irminger Sea and is found downstream, off the East Greenland shelf, between the Denmark Strait Overflow Water and the intermediate convective waters (Labrador Sea Water [LSW] and intermediate waters ventilated locally in the Irminger Sea).

Previous descriptions of the IC consist of velocities derived from surface drifters and float displacements, geostrophic velocities from summertime hydrographic sections referenced to Acoustic Doppler Current Profiler (ADCP) measurements, and altimetry. The drifter observations show that upper IC velocities can exceed 30 cm s^{-1} (Orvik & Niiler, 2002). Similar values, up to 25 cm s^{-1} averaged over the upper 200 m, were recorded by an ADCP underneath the container ship Nuka Arctica, which regularly transects the ridge since 1999 (Knutsen et al., 2005). Subsurface floats located at 700 m depth recorded speeds of 5–7 cm s^{-1} (Bower et al., 2002) and slower (<5 cm s^{-1}; Lavender et al., 2000), indicating that the flow is surface intensified. The shipboard ADCP data provided additional information about the horizontal structure. In these transects the IC exhibited a double velocity peak, spaced approximately 100 km apart, which was most pronounced in spring and disappeared in autumn (Knutsen et al., 2005). Våge et al. (2011) combined the same ADCP data with surface geostrophic velocities derived from altimetry and hydrographic sections to derive the mean full depth summer/autumn transport between 1991 and 2007. They defined between 500 and 700 km offshore of Cape Farewell as the IC and found a total transport of 19 ± 3 Sv ($1\ \text{Sv} = 10^6\ \text{m}^3\ \text{s}^{-1}$) for that area. For absolute

geostrophic velocities referenced to mean altimetry, they found an IC transport of 13 ± 3 Sv. However, the Våge et al. (2011) ADCP-referenced estimate is rather large also compared to more recent estimates by Sarafanov et al. (2012) who found 12.0 Sv, Chafik et al. (2014) 8.5 Sv, and Daniault et al. (2016) 9.5 Sv. These estimates all use slightly different methods, boundaries, and time periods, which complicates comparison.

The Irminger Sea is an important basin in terms of water mass transformation. Lozier et al. (2019) showed that the overturning across the OSNAP array east of Greenland is approximately seven times larger than overturning across the array west of Greenland and contained about 88% of the total variance. An unknown part of this overturning in the eastern Subpolar North Atlantic, which has the maximum of the stream function at lower densities than west of Greenland, takes place in the Irminger Sea. Deep convection has been observed in the center of the Irminger Sea during strong winters (2000, 2007–2008, 2012, 2015, and 2016; de Jong & de Steur, 2016; de Jong et al., 2012, 2018; Piron et al., 2015, 2017; van Aken et al., 2011). During the winter of 2007–2008 deep (1,000 m), mixed layers were seen as far east as 36°W, well outside the central Irminger Sea, and just west of the IC array. During the first OSNAP deployments described here, 2014–2015 and 2015–2016, record deep (>1,400 m) mixed layers were again observed in the central Irminger Sea. The Irminger Sea has now returned to a cold and fresh state.

Restratification of the Irminger basin with warmer, saltier water is thought to occur mainly through mesoscale processes. The IC was considered as a likely source of warm core anticyclones observed in the central Irminger Sea by Fan et al. (2013). They described an increase in salinity in anticyclone cores from 2002 to 2009, which possibly contributed to the basin-wide increase in salinity over this period (van Aken et al., 2011). Fratantoni (2001) analyzed velocities derived from surface drifters and identified a region of high eddy kinetic energy (EKE) west of the RR, concurrent with the IC. In altimetry data sets two bands of enhanced EKE are seen parallel to the RR (Volkov, 2004), one just east of the center of the Irminger Gyre and the other colocated with the IC. The seasonal EKE variability in the Irminger Sea was found to be small compared to the Iceland Basin and Labrador Sea. However, the interannual variability in EKE described by Volkov (2004) showed similarities with the multiyear variability of the IC transport as described by Våge et al. (2011), with lower values in the early 1990s and an increase toward the early 2000s. The presence of mesoscale activity is expected to contribute significantly to the transport variability of the IC on subseasonal time scales.

Until recently, high temporal resolution, full-depth, year-round observations of temperature, salinity, and velocity of the IC were not available. With the deployment of the IC array in the summer of 2014, as part of the larger OSNAP array (Lozier et al., 2017, 2019) this changed. The IC moorings provide the first near-continuous, full water column observations of direct (as opposed to geostrophic derived) IC velocities and hydrography. Here, we present volume, heat, and freshwater transports of the IC based on the first 2 years of OSNAP, from July 2014 to August 2016. This paper aims to describe the mean fields as well as the variability in transport and water mass transformation observed during these 2 years. This paper is organized as follows. The temperature, salinity, and velocity data obtained with the IC array, as well as the processing and interpolation methods, are presented in section 2. Further included in section 2 are subsections on the error estimation and the additional data used for analysis. In section 3, we detail the mean fields and the transport and quantify the ability of the array to capture the flow characteristics and variability using an ocean reanalysis product. This is followed by an analysis of the transport and hydrographic variability. In section 4 we discuss these findings, and section 5 finishes with the conclusions.

2. Data and Methods

2.1. Instrumentation

The IC mooring array was first deployed from the R/V Knorr on cruise KN-221-2 in July 2014. The IC array (Figure 1) consists of four tall moorings (IC1, IC2, IC3, and IC4) in the main IC and one short mooring (IC0) to the west to capture the deep flow of NEADW over the ridge. All five moorings were serviced and redeployed during R/V Pelagia cruise 64PE400 between 9 and 29 July 2015 and again during RSS Discovery cruise DY054 between 27 July and 17 August 2016. All moorings have been recovered and deployed in summer 2018 with the R/V Neil Armstrong and are planned to be recovered and redeployed with R/V Pelagia in summer 2020. The short western mooring, IC0, is located at the foot of the ridge and covers the water column from the bottom, at 2,940 to 2,250 m depth. The four tall moorings, consecutive named IC1 to

IC4, are located on the western flank of the ridge, between ~2,500 m depth and the top of the ridge at ~1,500 m depth. Each tall mooring extends from the bottom to 60 m below the surface to avoid damage by fishing activity. In addition, a tall mooring (called M1) of the US OSNAP program located on the eastern side of the top of the RR is included in the analysis (Figure 1). This eastern mooring allows us to determine the border between the northward flow and the southward flow, respectively, west and east of the RR ridge crest. Details of the mooring deployments (locations, depths, and time coverage) are given in Table S1 in the supporting information.

The short mooring, IC0, is equipped with Aanderaa recording current meters (RCM11) at 2,275 and 2,880 m, and with Sea-Bird Electronics SBE37 (MicroCATs) at 2,275 and 2,930 m, which record pressure, temperature, and conductivity. The four tall IC moorings are each equipped with an upward looking ADCPs (RDI 75 kHz Long Ranger ADCP) at a target depth of 475 m, which measures current speed and direction above the instrument up to approximately 50 m depth. At target depths of 725, 950, 1,450, 2,250, and 50 m above the bottom, single-point current meters (either RCM11 or Nortek Aquadopps) measure velocity. At 60, 475, 950, 1,450, and 2,250 m depth and at 50 m above the bottom, MicroCATs measure temperature, conductivity, and pressure. At roughly 180 m and at 725 m depth, Sea-Bird SBE56 thermistors provide additional temperature data in the thermocline. The M1 mooring is equipped with an upward looking ADCP at 300 m; Nortek Aquadopp current meters at 700, 1,200, 1,430, and 1,645 m; and MicroCATs at 50, 100, 200, 350, 500, 700, 900, 1,200, 1,430, and 1,645 m. Sampling rates are 1 hr for all ADCPs, 30 min for the current meters in the IC moorings, and 20 min for the current meters in the M1 mooring. The MicroCATs sample every 15 min and the SBE56 thermistors every 5 min in all moorings.

Data from an earlier nearby mooring deployment, from August 2003 to October 2004, are presented as well. These moorings were deployed as part of the Long-term Ocean Circulation Observation (LOCO) project with a focus on internal and tidal shear variability over a topographic ridge (van Haren, 2007) and hence the focus on the deep layers only. The LOCO array consisted of four moorings, each equipped with current meters (RCM11s and Valeports) and ADCPs below 1,000 m depth only. Vertical instrument spacing varied from ~100 m for the easternmost mooring and 400 m for the westernmost mooring. Sampling rates for the instruments in the LOCO moorings were hourly.

2.2. Mooring Data Processing

The recovery of instrument data was generally very good (100% for the ADCPs, 94% for the RCMs, 99% for the MicroCATs, and 100% for the thermistors). Treatment of small data gaps is described in the supporting information. All ADCP and current meter data were corrected for the magnetic declination at the mooring sites. The velocity data from ADCPs and current meters were filtered with a 41-hr low-pass centered Butterworth filter to remove tides and inertial motions and then daily subsampled. Vertical interpolation between instruments was done using Matlab's "pchip" interpolation, that is, a shape preserving piecewise cubic Hermite interpolant. The data were interpolated linearly horizontally on a grid with bottom-following contours. The horizontal grid distance was 2 km. The grid has a fixed number of layers, which increase in thickness in the east. This choice was made for two reasons: (1) to avoid empty bottom triangles between moorings located at different depths, (2) because the grid naturally aligns with the structure of the NEADW and the isopycnals over the RR. The vertical grid spacing was 10 m down to 1,300 m, and below that, the vertical grid distances followed the topography and varied from 55 m in the west (in the deep basin) to 15 m in the east (over the top of the RR). Varying the number of layers did not affect the results of the calculation. The velocities were rotated clockwise by 10° to obtain along ridge (V) and across ridge (U) velocities.

The MicroCAT data were calibrated against calibrated shipboard CTD casts before deployment and after recovery, and offsets or drifts in conductivity were corrected for and large spikes were removed. The 15-min interval MicroCAT temperature (T), salinity (S), and pressure (P) data, as well as the 5-min thermistor temperature and reconstructed pressure data, were filtered with a 41-hr low-pass symmetric Butterworth filter and regridded at hourly intervals. T and S data were extended to the surface using Argo seasonal climatologies and SST data (supporting information) and vertically interpolated using Matlab's "pchip" interpolation. The T and S profiles were interpolated horizontally on the same grid as the velocity data.

2.3. Transport Calculations

Transport estimates are derived for the daily fields. The volume transport is defined as

$$V(t) = \int_{X_w}^{X_e} \int_{bottom}^{surface} v(x, z, t) dz dx,$$

where *Xw* and *Xe* are the western and eastern boundary, respectively.

The heat (or temperature) transport is calculated with respect to a reference temperature of 0°C and is defined as

$$H(t) = \rho c_p \int_{X_w}^{X_e} \int_{bottom}^{surface} v(x, z, t) T(x, z, t) dz dx,$$

where ρ is density and c_p is the specific heat capacity.

The freshwater transport is calculated with respect to a reference salinity S_{ref} of 34.9189 (as used for OSNAP calculations; Lozier et al., 2019):

$$F(t) = \int_{X_w}^{X_e} \int_{bottom}^{surface} v(x, z, t) \left(1 - \frac{S(x, y, t)}{S_{ref}}\right) dz dx.$$

2.4. Error Estimation

The standard error of the transports is calculated as the standard deviation divided by the square root of the degrees of freedom (number of independent samples) of the time series. Additionally, a subsampling exercise using data from an ocean reanalysis was performed to estimate the sampling error. Velocity fields were downloaded from the reanalysis GLORYS12V1 hosted by the Copernicus Marine Environment Monitoring Service (CMEMS), which has a model component consisting of Version 3.1 of the NEMO ocean model (Madec et al., 2008) and is forced by atmospheric fields from the ECMWF (European Centre for Medium-Range Weather Forecasts) Integrated Forecast System (IFS). The reanalysis has a 1/12° horizontal resolution and 50 vertical levels, ranging from 1 to 5,500 m depth with a resolution of 1 m at the surface decreasing to 450 m at the bottom. The downloaded reanalysis daily time series covers the period from 1 July 2014 to 31 August 2016, covering the two mooring deployments. Transports are calculated from the full reanalysis fields as well as reanalysis fields subsampled at instrument positions and interpolated vertically and horizontally using the same methods as the mooring data.

2.5. Calculation of Seasonal Fields From Argo

To allow a comparison of seasonality in the 2-year IC array time series with average seasonality over a longer period, we derived seasonal (3-month average) *T*, *S*, and velocity fields from Argo and satellite altimetry data. To assure ample seasonal coverage by Argo, this was done for the more recent period 2012–2017, during which there were significantly more floats present year-round. The start point of January 2012 was also chosen to avoid aliasing of large interannual changes into seasonal fields, as basin-scale deep convection has been observed from the 2011–2012 winter onward (e.g., de Jong & de Steur, 2016; Fröb et al., 2016; Piron et al., 2015). Data were selected within 50 km of the IC array and were averaged on an 0.25° longitude grid with 10 m depth bins. Three-monthly mean fields of temperature, salinity, and geostrophic velocity, averaged over 2012–2017, were derived. At each grid point, the individual hydrographic records were inversely weighted by their deviation from the median value to exclude eddies and bad data. This prevented unrealistic gradients that would cause errors in the geostrophic fields. Geostrophic velocity from Argo field dynamic height was referenced to velocities from satellite altimetry averaged over the same months. As we will show later, these altimetry-derived velocities agree well with the velocities observed by the moorings. For this the Ssalto/Duacs altimetry product (MADT-UV) was obtained from the Copernicus Marine and Environment Monitoring Service (CMEMS, http://www.marine.copernicus.eu). Surface geostrophic velocities (2012–2017) were linearly interpolated from the original 0.1° grid onto the Argo longitude grid and then averaged into 3-monthly fields. Velocities were rotated by 9° to obtain an along-ridge orientation (positive velocity northward along the ridge). Lastly, IC volume transport from the Argo fields was calculated by integrating the velocity fields over depth (0 to 2,000 m) and

distance (from IC1 to IC4). These transports are compared to the transports from the IC mooring data integrated over the same depth and distance intervals.

2.6. Data From the Central Irminger Sea

To show water mass transformation in winter, we compare hydrographic properties recorded by the IC array with observation from the convective region in the central Irminger Sea. The Ocean Observatories Initiative (OOI) mooring is located at 59.98°N, 39.48°W (Figure 1) and recorded deep (1,600 m) mixed layers during the winters of 2014–2015 and 2015–2016 (de Jong et al., 2018). Data from the profiling CTD were obtained from the OOI data portal (at https://oceanobservatories.org/data-portal/). More details on instruments and data are described in de Jong et al. (2018).

3. Results From the IC Array

3.1. Mean Fields and Transports

The 2-year mean fields of conservative temperature, absolute salinity, and along-ridge velocity obtained from the IC moorings are shown in Figure 2. The mean temperature and salinity fields show the front associated with the warm and saline Irminger SPMW (García-Ibáñez et al., 2015) over the top of the RR. This warmer water continues cyclonically around the basin and joins the EGC as Irminger Water. Underneath this warm core (below 1,000 m), Icelandic Slope Water is found, which is formed in the northern Iceland Basin as a mixture of the saline Iceland Basin SPMW and colder, fresher overflow water coming over the Iceland Faroe Ridge (van Aken & de Boer, 1995). Toward the central Irminger Sea, these middepths are occupied by a fresher core of LSW, modified by local convection (de Jong et al., 2012, 2018; de Jong & de Steur, 2016; Piron et al., 2015). Below the LSW, the NEADW is characterized by lower temperatures and very homogeneous salinities.

The velocity field in Figure 2 shows two full-depth northward cores with surface intensified velocities. In the mean, the western core is located at IC1, while the eastern core is observed at IC3 and IC4. These cores are separated by a southward flow most often seen at IC2. This southward flow was termed a recirculation by Sarafanov et al. (2012). It appears to be associated with fresher waters at middepth, reminiscent of LSW. However, it is not yet clear whether this "recirculation" extends along the length of the RR or is an artifact of locally occurring eddies. Possibly eastward and southward velocities from eddies could draw water from the central Irminger Sea into the array. The near-surface velocities from the interpolated mooring data agree well with the mean surface geostrophic velocities derived across the array from altimetry (Figure 2). Overall, the moorings appear to be appropriately placed to capture both ICs cores. The extrapolation to the west of IC1 may slightly overestimate the velocities there. However, altimetry data show that the location of the zero crossing shown in Figure 2 is not fixed in time and therefore extrapolating the IC1 measurements to values equaling zero west of IC1 would oversimplify the circulation. For now, the extrapolation up to 200 km west of the top of the RR (marked by the triangle in Figure 2) is kept to facilitate comparison with earlier transport estimated over this region. The ability of the mooring array to fully capture the two IC cores is discussed in more detail in section 3.2.

In the deeper parts of the array we find NEADW. Recent studies suggest that the most of the NEADW from the Charlie Gibbs Fracture Zone continues westward (Zou et al., 2017, 2020) and that the NEADW in the Irminger Sea comes through RR fractures further north at the Bright Fracture Zone and other gaps (Bower & Furey, 2017; Kanzow & Zenk, 2014; Petit et al., 2019; Racapé et al., 2019). The NEADW located over the bottom is rather homogeneous, does not have a strong density gradient, and has only a very weak near-bottom velocity maximum (Figure 2c). Northward velocities in the near-bottom current meter (at 1960 m) in IC2 are slightly intensified (mean of northward velocities is 5.5 cm/s) with respect to those observed in the current meter mounted at 1,720 m depth (mean of 3.6 cm/s), while southward velocities are fairly similar (−2.3 and −2.4 cm/s, respectively). In this deep part of the array, we can compare the 2014–2016 data with the 2003–2004 deployment. Two deep (but weak) cores present in the 2014–2016 mean fields are also visible in the 2003–2004 data (Figure 2e). Weaker velocities are seen in between and further down the slope. At times, a recirculation similar to that observed in the IC array was seen extending over the middle two LOCO moorings (not shown), but this did not result in southward velocities in the 1-year mean field.

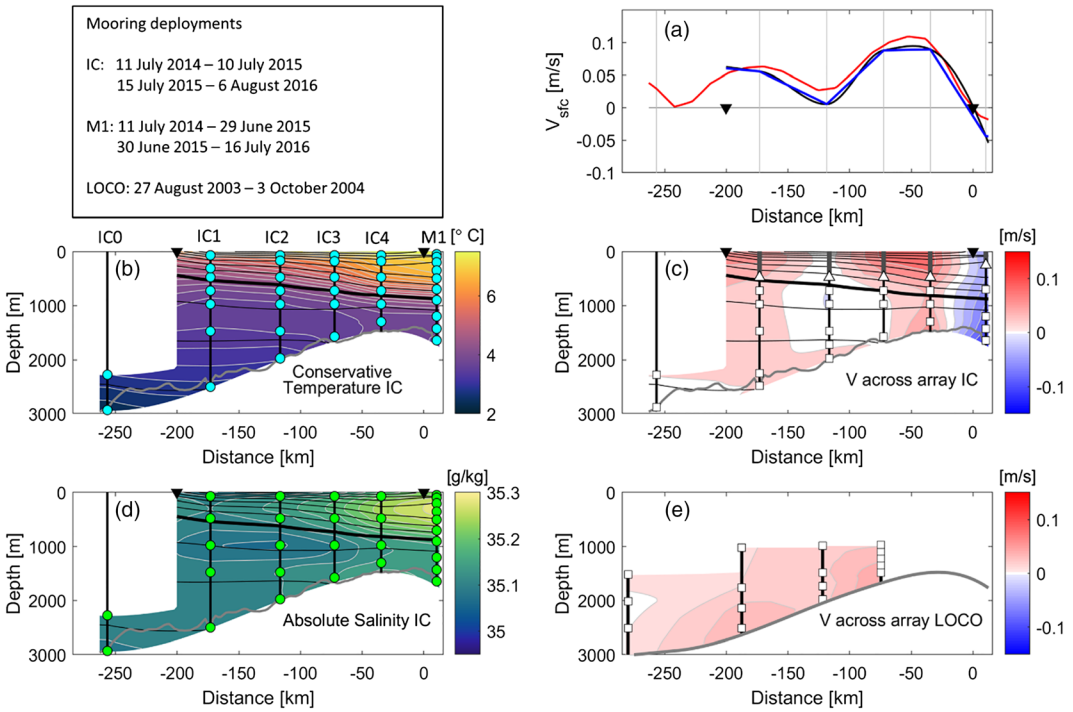

Figure 2. Table in upper left: dates of the mooring deployments. (a) Surface geostrophic velocities from altimetry averaged over the 2-yearlong deployment period (red) and linearly (blue) and spline (black) interpolated near-surface velocities averaged over the 2-year deployment period. Mooring positions are indicated with gray vertical lines, and black triangle markers indicate distance of 500 and 700 km from Cape Farewell. (b) Mean conservative temperature field from the IC array, isotherms contours are plotted every 0.2°C. MicroCAT and thermistor depths are indicated with cyan circles. (c) Two-year mean velocity field from the IC array; isotachs are plotted every 0.02 m/s; current meter depths are indicated with white squares. The upper 475 m is observed by ADCPs, indicated by the white triangles and thick gray lines. (d) Mean absolute salinity field from the IC array, isohalines are plotted every 0.02 g/kg. MicroCAT depths are indicated with green circles. Isopycnals of potential density reference to the surface are shown in black in b, c, and d at a 0.05 kg m^{-3} interval, with the 27.7 kg m^{-3} isopycnal drawn with a thick line. (e) One-year mean velocity field from the LOCO array; isotachs are plotted every 0.02 m/s; current meter depths are indicated with white squares.

For a quantitative comparison between the 2014–2016 IC data and the 2003–2004 LOCO data, we calculated the transport in the area of overlap between the two gridded data sets. The mean transport and standard deviation are 4.3 ± 2.1 Sv for the 2003–2004 period and 2.8 ± 2.6 Sv for the 2014–2016 period. The difference in these estimates may be caused by a shift of the location of the eastern velocity core. This core was located closer to the top of the ridge in the 2014–2016 deployment, and therefore outside the area of overlap with the 2003–2004 data, leading to a lower estimate of the deep transport.

The full-depth transport through the IC array was calculated over the region between 500 and 700 km from Cape Farewell, the same horizontal extent used by Våge et al. (2011). The 500 and 700 km boundaries are marked by triangles on the top axis in Figure 2. The mean transports are summarized in Table 1. The mean full-depth transport across the region between 500 and 700 km is 10.6 Sv, with a standard deviation of 9.2 Sv (4.4 Sv) for the daily (monthly) transport values. The mean heat transport through the array is 0.21 ± 0.18 PW, and the northward freshwater transport relative to the OSNAP reference salinity (34.9189) is negative, −22.5 ± 20.3 mSv, due to the saline nature of the IC.

The standard error associated with the 2-year mean volume transport is obtained from the standard deviation divided by the square root of the number of independent samples (n). With 736 daily values and a decorrelation time scale of 18 days, we have $n = 736/18 = 41$ independent samples. Hence, the standard error for volume transport amounts to $9.2\ \text{Sv}/\sqrt{41} = 1.4$ Sv. Standard errors associated with the 2-yearlong mean heat transport are 0.028 PW and 3 mSv, respectively. These standard errors are much smaller than the standard deviation of the time series, which is 9.2 Sv for the daily values and 4.4 Sv for the monthly values. However,

Table 1
Two-Year Mean and Standard Deviation of Daily Time Series of Volume, Heat, and Freshwater

	Mooring data			Reanalysis data	
	Volume (Sv)	Heat (PW)	Freshwater (mSv)	Volume (Sv) full	Volume (Sv) subsampled
Total	10.31 ± 9.45	0.20 ± 0.18 (0.98)	−19.9 ± 21.5 (−0.81)	12.14 ± 4.84	10.7 ± 6.52
IC1 to 0 contour	7.39 ± 7.22	0.15 ± 0.14 (0.99)	−15.9 ± 15.1 (−0.86)	7.91 ± 3.25	7.85 ± 4.69
500 to 700 km	10.61 ± 9.16	0.21 ± 0.18 (0.98)	−22.5 ± 20.3 (−0.81)	10.3 ± 4.52	10.65 ± 6.36
500 to IC2 (WB)	5.26 ± 6.89	0.09 ± 0.12 (0.99)	−6.5 ± 9.3 (−0.93)	2.19 ± 3.06	3.27 ± 4.37
IC2 to 700 (EB)	5.35 ± 5.79	0.12 ± 0.13 (0.99)	−16.0 ± 18.0 (−0.87)	8.12 ± 3.44	7.38 ± 3.81

Note. For freshwater transport reference salinities of 34.9189 (OSNAP) are used. The correlation of the heat and freshwater transport with the volume transport is given between brackets. Values are given for different horizontal extends of the Irminger Current as well as separately for the eastern branch (EB) and western branch (WB). For comparison the volume transport for the full and subsampled reanalysis field is also given.

as we will show in the next section, the small standard error is representative for the array's ability to accurately capture the IC and its variability. Rather, the high standard deviation highlights the strong variability of the IC (discussed further in section 3.3), which has important implications for the interpretation of synoptic transport estimates.

The transport by the two separate IC cores was calculated using both flexible and fixed core boundaries to account for their shifts in position in time. The fixed boundary is based on the mean field; it separates the western and eastern core, respectively, into the region from 500 km to IC2 and from IC2 to 700 km from Cape Farewell (Figure 2). This results in a nearly equal division of the mean transport (5.3 Sv west and 5.4 Sv east) between the cores. For the flexible boundary definition, the position of the minimum velocity between the cores at each time step determines the dividing line between the cores. For the outer boundaries, on the west side of the array and over the ridge between the IC and the ERRC, the position of the zero velocity contours are used. The boundary between the IC and ERRC was found to have the least variability. At time steps when no clear boundary can be defined according to these definitions, the default values are those determined from the mean field. The mean core transports derived with these flexible boundaries are 5.7 ± 5.6 Sv for the eastern core and 5.9 ± 7.2 Sv for the western core. The higher transports, compared to the fixed core definitions, are mainly the result of exclusion of occasionally strong southward flow on the eastern and western boundaries. However, the correlations between the transport time series of the fixed and flexible core definitions are very high (0.99; all given correlations are significant at the 99% level), which gives confidence that the fixed boundaries are an adequate first approximation. Using these fixed boundaries, we find a slightly higher heat and salt transport in the warmer and saltier eastern core (0.12 PW and −16.0 mSv in the east vs. 0.09 PW and −6.5 mSv in the west).

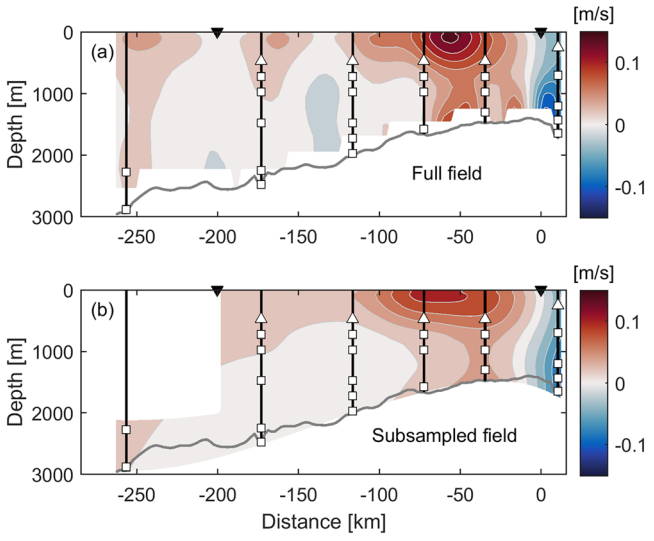

Figure 3. (a) Mean velocity of full reanalysis field. (b) Mean field of velocity subsampled at instrument locations and subsequently interpolated.

3.2. Ability of the IC Array to Capture the Current

Although the design of the array is based on existing observations of the IC structure, we investigate whether the resolution provided by the instrumentation on the moorings is indeed adequate to capture the mean state as well as the variability of the IC. We use the CMEMS ocean reanalysis, described in section 2.4, which has a (1/12)° (<5 km) resolution that resolves mesoscale variability. The full reanalysis fields are compared to fields subsampled at the moored instrument positions, which are subsequently interpolated in the vertical and horizontally similar to the mooring data. This is similar to the analysis done by Li et al. (2017) for the full OSNAP array.

The mean fields of the full reanalysis fields show a two-core structure in the upper water column (Figure 3a) that is very similar to both previous observations (section 1) and the observations from the IC array (Figure 2). The subsampled/interpolated reanalysis field (Figure 3b) recreates the main features of this field. Compared to the reanalysis data, the moorings have a lower horizontal resolution which makes the velocity field appear smoother. The location of the southward flow is shifted

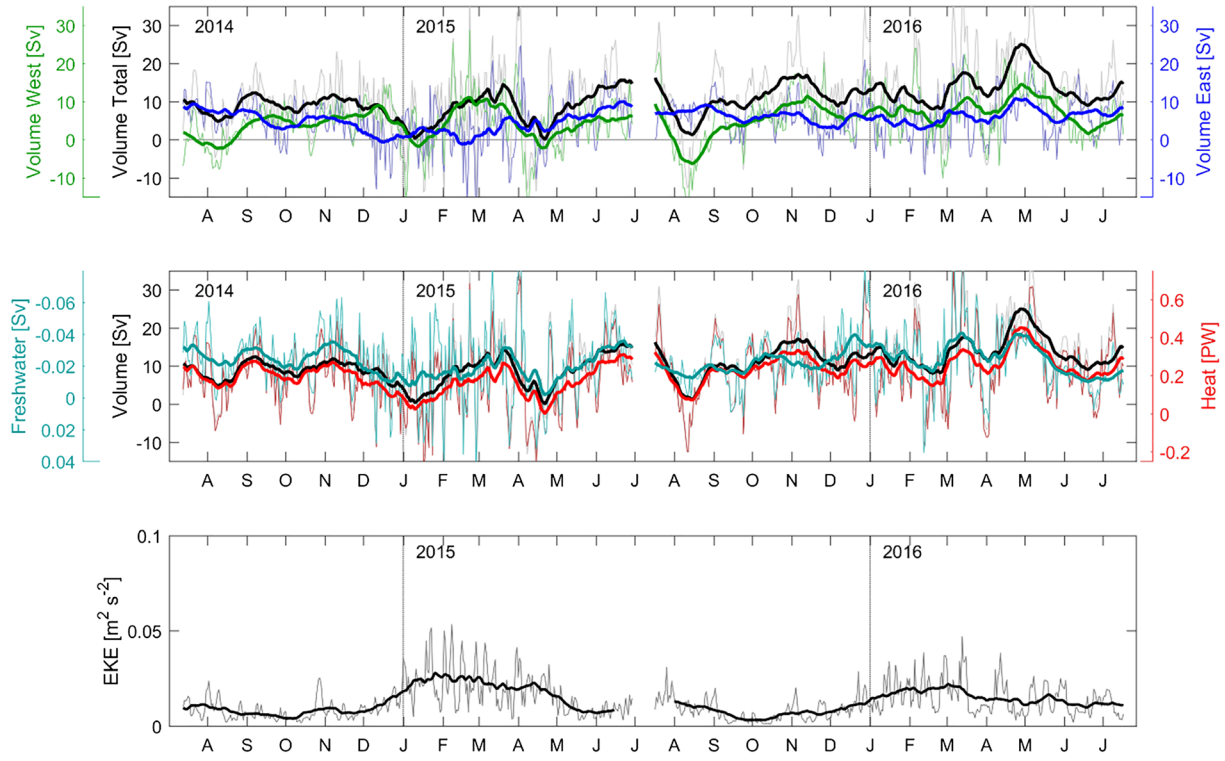

Figure 4. Top: time series of volume transport between 500 and 700 km from Cape Farewell (black) and separation into western (green) and eastern branch (blue). Middle: time series of volume (black), heat (red), and freshwater (cyan) transport over 500 to 700 km region. Bottom: EKE obtained from near surface velocities and averaged over 500 to 700 km region. Thick lines are smoothed with 30-day filter. Note that the freshwater transport axis is reversed.

somewhat compared to the observations, where it is captured by the moorings. The mean transport calculated between 500 and 700 km (Table 1) from the full field is 10.3 Sv and from the subsampled fields is 10.6 Sv, which is similar or very close to the observed 10.6 Sv. The correlation between the 2-year time series of the full field transport and the subsampled transport is also high (0.84), which gives confidence in the array's ability to capture the variability of the flow as well as the mean. The low standard error calculated from the observations (1.3 Sv) and the small difference (0.3 Sv) between transports from the full and subsampled reanalysis fields highlight the strong variability of the IC as represented by the much larger standard deviations of the daily (9.2 Sv) and monthly (4.4 Sv) time series.

3.3. Transport Variability

The high variability is clearly visible in the daily and 30-day smoothed time series of volume, heat, and freshwater transport in Figure 4. Again, transports are integrated between 500 and 700 km from Cape Farewell and over the full depth range. The transports for the fixed current boundaries for the western and eastern cores, defined as the regions from 500 km to IC2 and from IC2 to 700 km, are also shown. Both cores contribute to the high IC variability, but the western core has a slightly higher correlation to the total transport than the eastern core (R_{west} is 0.78 vs. $R_{east} = 0.66$). There is no (negative) correlation between the transport of the two cores themselves, and thus, they do not compensate each other. The overall variability in the heat transport is mainly driven by that of the volume transport ($R = 0.98$), while the variability in salinity fields has a slightly larger role in the (negative) freshwater transport ($R = -0.81$).

In order to identify coherent patterns of variability in transport, we performed an empirical orthogonal function (EOF) analysis on the daily velocity fields for the first five principle components (PCs). The EOF analysis computes the eigenvectors of a spatially weighted anomaly covariance matrix of the data. The corresponding eigenvalues provide a measure of the percent variance explained by each pattern (Zhang & Moore, 2015). Figure 5 shows the first four orthogonal modes, which together contain 93% of the variability. These patterns highlight the strong vertical coherence in variability in the water column. The center of the

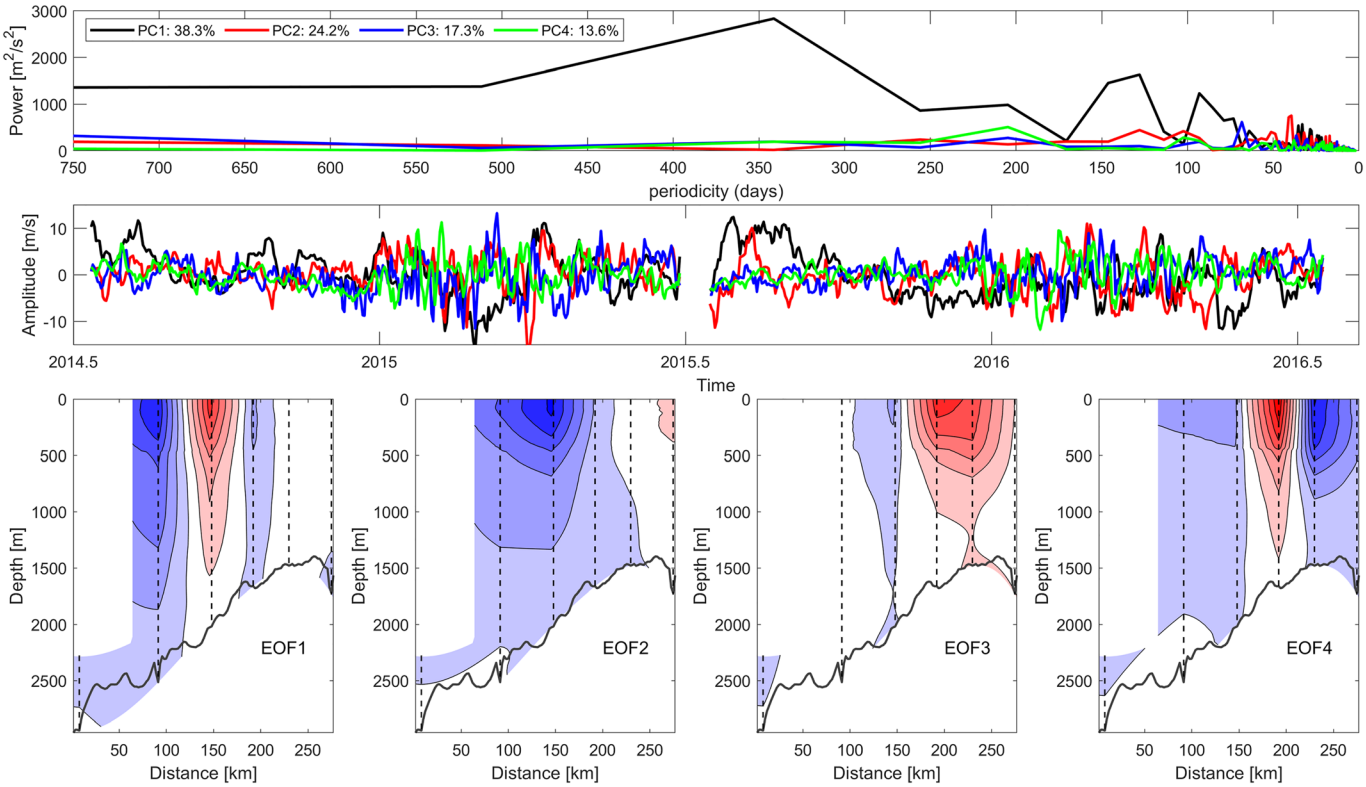

Figure 5. Results of the EOF analysis of the velocity field using the first four components. Power spectra of the four PCs are displayed in the upper panel and their respective time series in the middle panel. The patterns of the four EOFs are shown left to right in the panels below.

tripole in the first EOF corresponds to the location of the southward flow at IC2 and contains 38.3% of the variability. It occurs at the lowest frequencies, with spectral peaks in this PC at periods of 341, 128, and 93 days. The second EOF contains 24.2% of the variability and corresponds to the western branch around IC1 and IC2. The third EOF (17.3%) corresponds to variations in strength of the eastern branch as a whole. Both the PCs of the second and third EOF have spectral peaks at higher frequencies, with periods of 39 (second) and 68 (third) days or less. The fourth PC (13.6%) expresses variability of the position of the eastern core between IC3 and IC4. This PC has a peak at lower frequencies (204 days).

These modes of variability correlate with transports in the respective cores. The first PC is correlated negatively ($R = -0.56$) with the transport in the western branch and reflects lower transports in the western core at time of fast southward flow at IC2. The second and third PCs are strongly (0.83 and 0.84) correlated to the western and eastern core transports time series, respectively. The fourth PC does not have a strong correlation with any of the transports time series mentioned above but does correlate with the transport over the top of the ridge, integrated between IC4 and M1 ($R = -0.50$) likely increasing transport in this sector when the core moves to IC4. PC4 displays a high variability in winter and low variability in summer more clearly than any of the other PCs or transports (although PCs 2 and 3 show it slightly). High winter variability is also seen in the EKE time series (Figure 4) and may resemble the seasonal variability in atmospheric forcing in this region. This is subject to further investigation. To investigate the variability on even shorter time scales, we derived the energy spectra of 50-day high-pass filtered velocity time series (supporting information). The upper ocean variance is the highest between 9 and 42 days, and the first deployment period is slightly more energetic than the second period (Figure S1).

Looking at seasonal time scale, the 2-year time series is too short to compile a climatology, but some changes between seasons are clearly visible. Figure 6 shows 3-month average velocity and density fields, starting with the July–September (JAS) mean of 2014 and ending with the April–June (AMJ) mean of 2016. The 3-month periods were chosen so that the winter months with the strongest air-sea fluxes and mixing (JFM) are

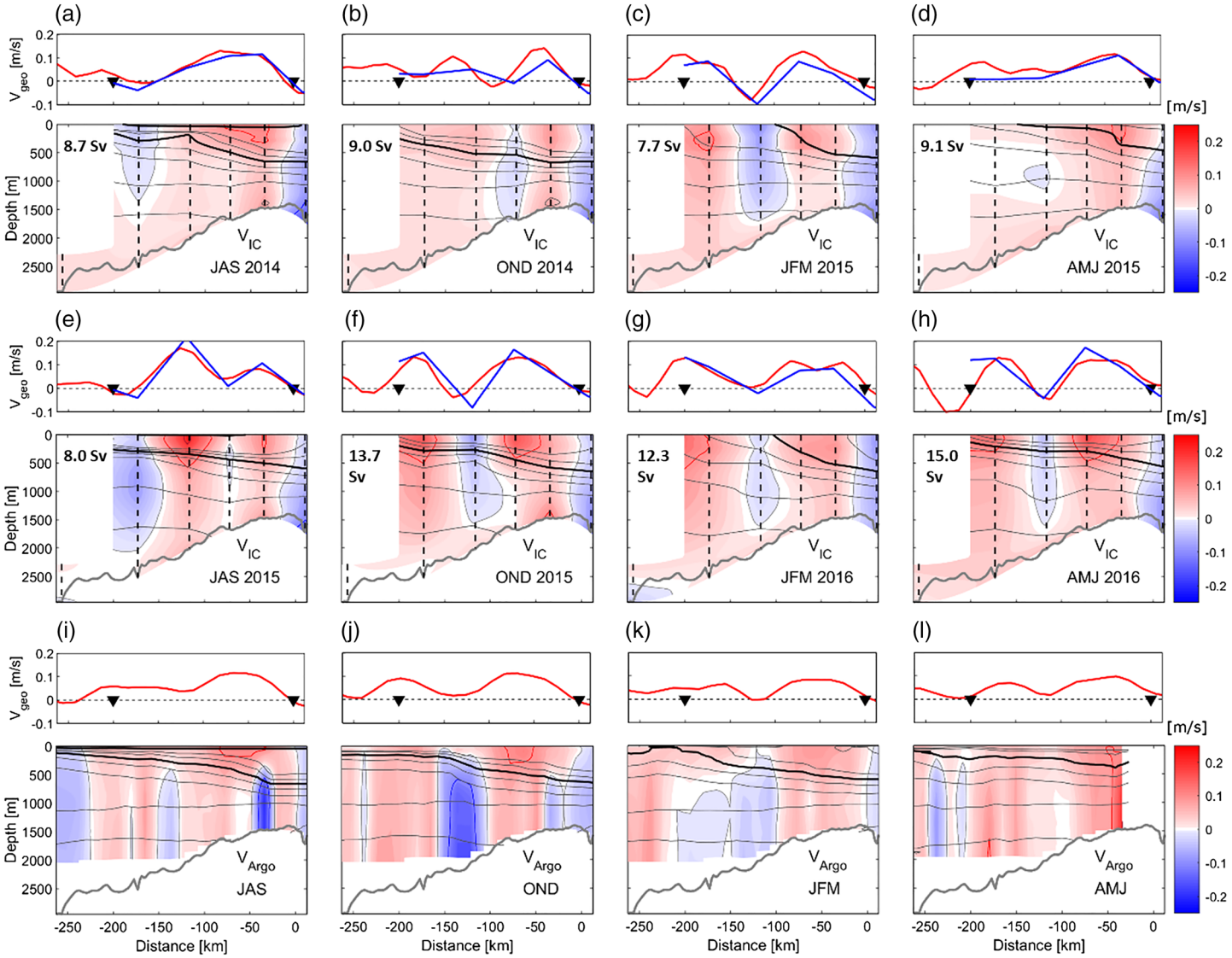

Figure 6. Mean velocity (color map) and density fields (gray contours) for consecutive 3-month periods of the mooring deployment with respective mean volume transport (a–h) and climatological (2012–2017) 3-month average of the velocity and density fields derived from Argo and altimetry (i–l). Dashed lines indicate mooring positions, and the thick black contour denotes the 27.7 kg m^{-3} isopycnal. Red (blue) lines mark the 0.1 (−0.1) and 0.2 (−0.2) m/s contour lines, respectively. Mean geostrophic velocities from altimetry, derived for the same period, are shown on top of each panel in red, with the near surface velocities from the moorings in blue. Seasonal mean transports of the IC velocity fields are shown in the upper left of the panels.

grouped together. In both summers (JAS), strong southward flow is observed at IC1, while IC2 through IC4 mainly show northward flow. The strong southward flow at IC1 results in lower integrated transports through the array from 500 to 700 km from Cape Farewell, estimated at 8.7 Sv for JAS 2014 and 8.0 Sv for JAS 2015. In autumn (OND) and winter (JFM) the IC is separated into two distinct cores, with strong northward transport at IC1 and IC4, while a weaker recirculation is present at IC2 or IC3. Overall, this increases the transports in autumn to 9.0 Sv in OND 2014 and 13.7 Sv in OND 2015 (Figure 6). Transports in winter are somewhat lower, 7.7 Sv in JFM 2015 and 12.3 Sv in JFM 2016. In spring (AMJ), the recirculation appears to weaken, and the IC seems to transition to the single core observed in summer. In both years, the strongest values are seen in spring, with 9.1 Sv in AMJ 2015 and 15.0 Sv in AMJ 2016. Averaged over the 2 years, the seasonal cycle is 10.2 (JFM), 12.3 (AMJ), 8.6 (JAS), and 10.7 Sv (OND). Although the seasonal behavior is similar in both years, the transports are significantly larger from autumn to spring in the second deployment year, 2015–2016. This is mainly caused by stronger upper

ocean (<500 m) velocities throughout the second deployment. As a result, the transport averaged over each deployment separately is 8.6 Sv for 2014–2015 and 12.4 Sv for 2015–2016. The increase in transport could be related to a strengthening of the density gradient over the basin and over the array from the first deployment to the second. The density gradient (taken at 200 m) between the central Irminger Sea (at the OOI profiling mooring) and the top of the RR (at IC4) increased by about 20% and the gradient over the IC array (between IC1 and IC4) increased by about 35%. This difference seems mainly due to a larger remaining gradient at the end of the winter of 2015–2016, as we will discuss in the next section.

Figure 2 showed that the 2-year mean geostrophic velocities from altimetry agree well with the near-surface mooring observations. Similarly, the 3-month mean geostrophic and observed velocities also agree (Figure 6), although sometimes they do not overlap on the western edge. We used the 2012–2017 seasonally averaged velocities from altimetry to reference velocities from dynamic height fields from seasonal 2012–2017 Argo data (Figure 6). The 2012–2017 seasonal altimetry velocities are smoother than the seasonal profiles from the 2014–2016 period but show a similar seasonal shifting of the western core. Transports for these Argo fields and the IC fields were calculated for the water column above 2,000 km depth. Seasonal Argo transports are 4.1 (JFM), 12.7 (AMJ), 6.6 (JAS), and 1.3 Sv (OND), while the IC field yields to 9.4 (JFM), 11.3 (AMJ), 8.0 (JAS), and 10.0 Sv (OND). The Argo estimates are lower due to the smoother/lower surface velocity profiles (except for spring) but do show similar seasonal behavior with spring as the strongest transport season. Again, this is possibly related to density gradients set up by convection through winter. The seasonal cycle of the IC will be investigated in more detail as the record gets longer.

3.4. Hydrographic Variability

Some seasonal changes in hydrography, mainly the evolution of deep convection through winter (de Jong et al., 2012, 2018; de Jong & de Steur, 2016; Piron et al., 2015), have been described for the central Irminger Sea. However, much less is known about hydrographic changes through winter over the RR. Time series of temperature, salinity, and density at discrete depths for each of the tall IC moorings are shown in Figure 7. These hydrographic measurements show local wintertime modification of the upper layers. This modification through winter mixing occurs over the full width of the IC mooring array, and properties appear to be homogenized down to at least 400 m at IC1. This mixing is mostly confined to densities less than 27.7 kg m^{-3}, which are densities commonly associated with the Irminger Water and Irminger Rings found downstream (de Jong et al., 2014). Warming of the upper water column, and thereby most of the restratification, occurs through spring and summer.

Figure 7 shows the change in properties in T and S space for the outer tall IC moorings (IC1 and IC4) as well as for the OOI mooring. Monthly mean properties for the October months, which have on average the lowest monthly mean density, and April months, with highest monthly mean density, are highlighted. The scatter plot shows the progressive water mass transformation occurring in the Irminger Sea: from the warm, saline SPMW in the boundary current (at IC4) to the fresher but colder and denser water in the interior (at OOI). At the IC moorings, nearly all of the transformation to higher densities takes place in the layer of Irminger SPMW (or Irminger Water), above the 27.7 kg m^{-3} isopycnal, and across the isopycnal associated with the maximum of the stream function in the OSNAP East array (27.53 kg m^{-3}; Lozier et al., 2019). At OOI, the transformation is constrained to a much narrower density range, mainly between 27.7 and 27.75 kg m^{-3}. Similar maximum densities were reached in the winter of 2014–2015 and 2015–2016 in the central Irminger Sea and the western side of the IC array (Figure 7). However, at the two easternmost IC moorings (IC3 & IC4), the first winter resulted in significantly higher densities, with the lower densities in the second winter likely due to the weaker surface forcing in 2015–2016 (de Jong et al., 2018; Josey et al., 2019) and the fresh anomaly appearing in the upper layers (Holliday et al., 2020). As mentioned earlier, this smaller density gradient between the central Irminger Sea and the IC during the first year may account for the difference in transport between the first and second deployment.

The fresh signal in Figure 7 was seen over most of the hydrographic survey that was part of the mooring service cruise on the RRS Discovery (Holliday et al., 2018), and its origin has been discussed by Holliday et al. (2020). In the Irminger Sea, lowest salinities (outside of the East Greenland Current) were encountered at the positions of IC2 and IC3 (SA 34.83/SP 34.66). A collection of Argo profiles gathered for the region 35–31°W and 58.5–59.5°N between January 2003 and June 2018 indicates that salinities in the upper 50 dbar reached as low as 34.76 (SP 34.6) in September 2016 and August 2017, lower than the anomaly observed in

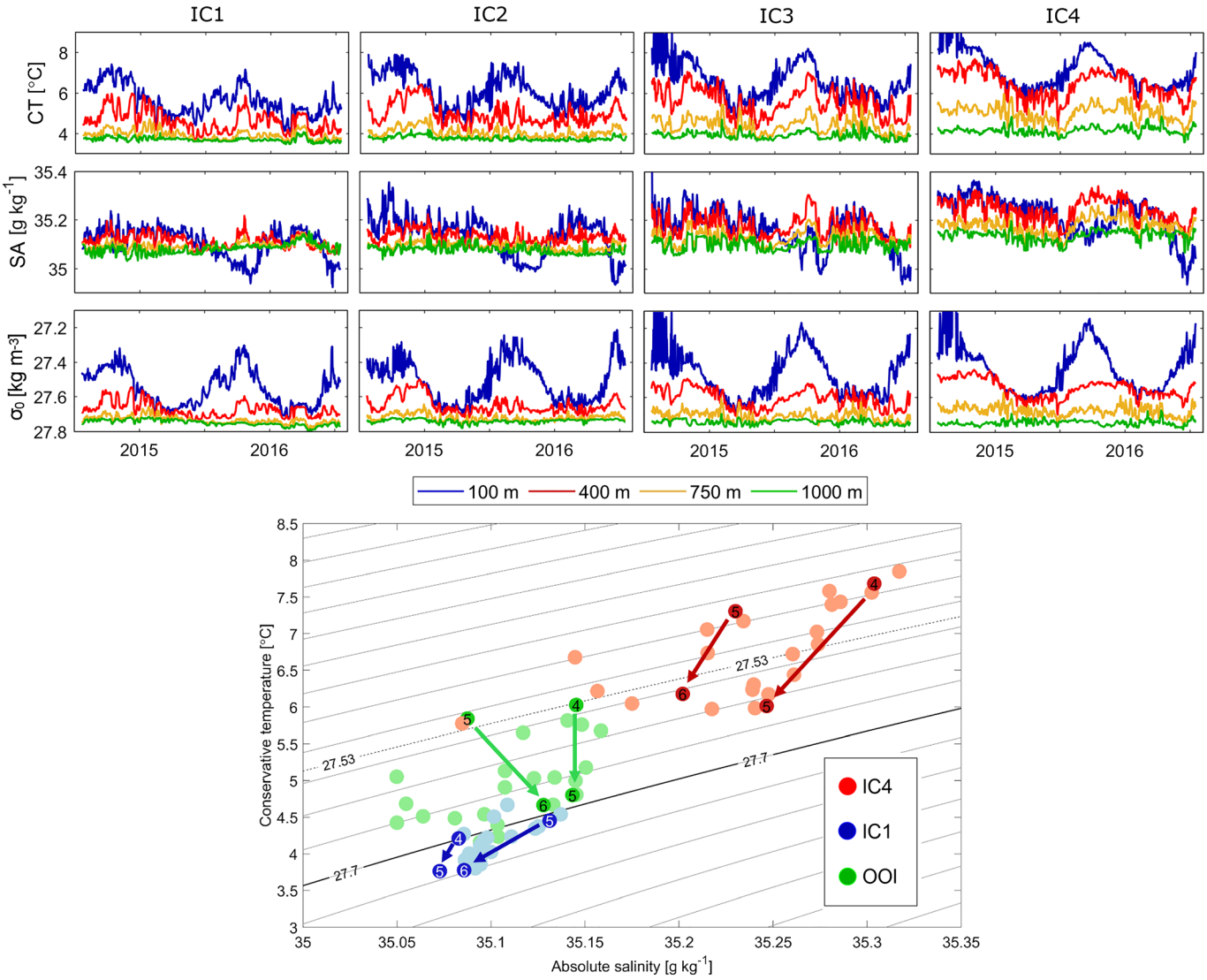

Figure 7. Time series of conservative temperature (*CT*, top row), absolute salinity (*SA*, second row), and potential density (σ_0, *y* axis reversed, third row) from the four tall IC moorings. Plotted are the depths levels of 100, 400, 750, and 1,000 m from the vertically interpolated profiles. Bottom panel: monthly mean *CT* and *SA* at 250 m depth for the outer two tall IC moorings and the OOI mooring. April, densest on average, and October, most buoyant on average, indicated with darker filled markers (specific year indicated with final digit). Transformation through winter indicated with arrows. The 27.7 and the 27.53 kg m^{-3} isopycnals are indicated with the bold and dashed lines, respectively.

2010 (Oltmanns et al., 2018), and appears to extend further east, although the fewer number of Argo profiles in 2010 gives some room for uncertainty here.

4. Discussion

The IC transports Irminger Subpolar Mode Water and NEADW northeastward along the RR. The flow of warm and saline water in the upper layers contributes to the heat and salt transport of the AMOC in the subpolar gyre. Since July 2014, the contribution of these transports to the overturning of the subpolar gyre is measured with the IC mooring array as part of the larger OSNAP array. The results presented here provide the first year-round record of transport over the west flank of the RR. The large variability seen in transports and the local water mass modification are important for the interpretation of previous synoptic transport estimates and for understanding the role of the Irminger Sea in the overturning in the North Atlantic subpolar gyre.

These new measurements show that while the structure of the mean IC velocity field observed by the IC array agrees with previous observations (Chafik et al., 2014; Daniault et al., 2016; Knutsen et al., 2005; Våge et al., 2011), this structure changes significantly on seasonal and shorter time scales. In the mean, the zero velocity contour, which delimits the northeastward IC from the southwestward ERRC, is found above the top of the ridge mid-way between the IC array's easternmost mooring (IC4) and the ERRC's array's westernmost mooring (M1). The eastern IC core is found just off the top of the ridge near the IC3 and IC4 moorings. On average the western IC core is located at IC1, but its location is highly variable, and its boundary is not well defined. A southward flow or recirculation is present in the mean at IC2 but seems to shift westward to IC1 in summer. Deep northward velocities associated with NEADW are found over the width of the array. To facilitate comparisons with earlier estimates, transports through the array were derived by integrating the observed velocities vertically and horizontally over the area between 500 and 700 km from Cape Farewell, from 34.15°W to 30.71°W. The mean transport over this 2014–2016 period is 10.6 Sv with an estimated error of 1.4 Sv. Both current cores contribute equally to the mean volume transport, 5.4 ± 5.8 Sv (east) and 5.3 ± 6.9 Sv (west). The total mean transport agrees with other recent multiyear estimates. Daniault et al. (2016) estimated a transport of 9.5 ± 3.4 Sv between 35.36°W and 31.06°W from six sections observed from 2002 to 2012. Chafik et al. (2014) calculated transports based on ADCP sections from the Nuka Arctica between 1999 and 2002 and found a transport of 8.5 ± 1.5 Sv in the upper 400 m west of the RR. They state that most of this transport (5 Sv) was found within 150 km of the ridge crest, which agrees with the 5.4 Sv we find for the eastern branch.

However, the studies above relied on sparse data over a longer time period averaged into one transport estimate. The high temporal resolution of the IC array shows that the range of variability is large, with monthly mean transports between 0.15 and 25.0 Sv and daily mean transports between −15.3 and 41.5 Sv. The small standard error, as well as the good fit from the reanalysis subsampling experiment, supports that these large ranges are indeed the results of transport variability rather than sampling errors. This puts estimates from synoptic measurements into context. A recent study by Petit et al. (2019) estimated the transport through three sections at different latitudes across the RR. They estimated a much larger transport of 23.5 Sv flowing through the OVIDE section, which overlaps with the IC moorings. Smaller transports were found through a section to the south (9.8 Sv) and through a section to the north (15.7 Sv). Petit et al. (2019) used these transports, as well as transports observed to cross the RR, to derive a direct inflow of 11.1 Sv from the IC into the central Irminger Sea. Although these observations are extremely useful to understand the local circulation, the mean transport that takes this route may be substantially smaller.

Heat and freshwater transports are also estimated to understand the role of the IC in the overturning circulation. The total heat transport is 0.21 PW, which is a significant contribution of the total heat transport through OSNAP east of 0.38 PW (Lozier et al., 2019). Freshwater transport was calculated with the OSNAP reference salinity (34.9189; Lozier et al., 2019), which is low compared to the salinity of the SPMW and NEADW found in the IC. This leads to a mean freshwater transport of −22.5 mSv. Due to the sloping front, the eastward current branch is warmer and more saline, thus making a larger contribution to the total heat and freshwater transport. The eastern (western) branch contributes 0.12 PW (0.09 PW) and −16.0 mSv (−6.5 mSv). The variability of the overall transport is largely determined by the western branch, where the minima in the total transport reflect minima in this western branch. There appears to be no compensation between the two cores, nor do they strengthen and weaken together.

Winter time transformation of water masses (convection) was found in the upper 400 m during the winter of 2014–2015 and somewhat shallower in 2015–2016. This mainly affects the Irminger SPMW, which is seen to cool and densify, approaching values seen in the central Irminger Sea. Since nearly all of this transformation at the IC array occurs in the 27.2 to 27.7 kg m^{-3} density range, it contributes to the overturning across the OSNAP east line. Deep convection (800 m) has been observed before this far east of the center of the Irminger gyre (de Jong et al., 2012); however, this may only occur in exceptionally strong winters such as those seen in 2014–2015 and 2015–2016 (de Jong et al., 2018; de Jong & de Steur, 2016; Josey et al., 2019) and 2008–2009 (de Jong et al., 2012). Seasonal estimates of transport from the IC measurements and the Argo-derived climatology suggest that winter modification of the density gradients within the basin strengthen IC transport in spring.

5. Conclusions

The first 2-year record from the IC array and the westernmost ERRC array mooring, from July 2014 to July 2016, was used to estimate the transport over the western flank of the RR. Data from 5 ADCPs, 22 current meters, 30 Microcats, and 4 thermistors were interpolated vertically and horizontally. The mean volume transport between 500 and 700 km from Cape Farewell, or 0 and 200 km west of the top of the RR, was found to be 10.6 Sv with a standard deviation of 9.2 Sv (4.4 Sv) for the daily (monthly) means. This estimate is similar to previous estimates (Chafik et al., 2014; Daniault et al., 2016). The transport is located in two cores, which are well resolved by the array. Both cores contribute equally to the mean transport, but the western core dominates the variability. The position of the southward flow, visible in the mean, is not stable and moves seasonally. Overall, the IC transport is highly variable, with strong southward transport (−15.3 Sv) as well as strong northward transport (41.1 Sv) seen at times. Spectra of high-pass (< 50-days) filtered current meter records show peaks between 9 and 42 days, while the PCs of EOF show peaks between 1 year and 40 days. Seasonal analysis suggests that transports are strongest in spring. A significant difference in transport was also seen between the first and second year of the deployment, from 8.6 to 12.5 Sv, likely related to an increase in the density gradient over the eastern Irminger Sea. Conversely, the EKE peak in the second winter, as well as higher frequency spectral peaks in individual current meters, was much lower than during the first, suggesting that mesoscale activity took energy out of the mean flow in the first year.

During the strong winters of 2014/2015 and 2015/2016, the upper 400 m of the water column was modified locally by convection, causing the 27.7 km m^{-3} to outcrop in the middle of the array. This water mass transformation during winter is likely to occur along the entire eastern side of the Irminger Basin during strong winters, until these waters finally subduct beneath the East Greenland Current and contribute to the overturning on the OSNAP East line. The IC mooring array is planned to continue, with the next recovery and redeployment in summer of 2020. The growing time series will allow further investigation into the interannual and seasonal variability of the IC.

Data Availability Statement

The following data sets were used in this study and are publicly available as:

de Jong M.F., & de Steur, L. (2019), Cruise 64PE400: Hydrographic survey of the Irminger Sea in July 2015 for the Overturning in the Subpolar North Atlantic Program (OSNAP). *SEANOE*. https://doi.org/10.17882/59302

de Steur, L., & de Jong, M.F. (2018), High-resolution current meter and hydrographic data from the Irminger Current mooring array 2014–2015. *NIOZ Royal Netherlands Institute for Sea Research*. https://doi.org/10.4121/uuid:77b2c4fc-c253-4,494-91bd-8d1ef66a014a

de Steur, L., & de Jong, M.F. (2018), High-resolution current meter and hydrographic data from the Irminger Current mooring array 2015–2016. *NIOZ Royal Netherlands Institute for Sea Research*. https://doi.org/10.4121/uuid:9ae97ceb-39e4-43ec-abdb-614103285c16

Acknowledgments

We acknowledge fieldwork support provided by the officers, crews, and technicians of the R/V Knorr, R/V Pelagia, and RRS Discovery. This project was funded by the European Union 7th Framework Programme (FP7 2007-2013) under Grant 308299 (NACLIM) and the Horizon 2020 Research and Innovation Program under Grant 727852 (Blue-Action).

References

Bower, A., & Furey, H. (2017). Iceland-Scotland overflow water transport variability through the Charlie-Gibbs Fracture Zone and the impact of the North Atlantic Current. *Journal of Geophysical Research: Oceans*, *122*, 6989–7012. https://doi.org/10.1002/2017JCO12698

Bower, A. S., Le Cann, B., Rossby, T., Zenk, W., Gould, J., Speer, K., et al. (2002). Directly measured mid-depth circulation in the northeastern North Atlantic Ocean. *Nature*, *419*(6907), 603–607. https://doi.org/10.1038/nature01078

Brambilla, E., & Talley, L. D. (2008). Subpolar mode water in the northeastern Atlantic: 1. Averaged properties and mean circulation. *Journal of Geophysical Research*, *113*, C04025. https://doi.org/10.1029/2006JC004062

Chafik, L., Rossby, T., & Schrum, C. (2014). On the spatial structure and temporal variability of poleward transport between Scotland and Greenland. *Journal of Geophysical Research: Oceans*, *119*, 824–841. https://doi.org/10.1002/2013JC009287

Cuny, J., Rhines, P., Niiler, S., & Bacon, S. (2002). Labrador Sea boundary currents and the fate of the Irminger Sea water. *Journal of Physical Oceanography*, *32*, 627–647. https://doi.org/10.1175/1520-0485(2002)032<0627:LSBCAT>2.0.CO;2

Daniault, N., Mercier, H., Lherminier, P., Sarafanov, A., Falina, A., Zunino, P., et al. (2016). The northern North Atlantic Ocean mean circulation in the early 21st century. *Progress in Oceanography*, *146*, 142–158. https://doi.org/10.1016/i.pocean.2016.06.007

de Boisséson, E., Thierry, V., Mercier, H., Caniaux, G., & Desbruyères, D. (2012). Origin, formation and variability of the subpolar mode water located over the Reykjanes Ridge. *Journal of Geophysical Research*, *117*, C12005. https://doi.org/10.1029/2011JC007519

de Jong, M. F., Bower, A. S., & Furey, H. H. (2014). Two years of observations of warm core anticyclones in the Labrador Sea and their seasonal cycle in heat and salt stratification. *Journal of Physical Oceanography*, *44*, 427–444. https://doi.org/10.1175/JPO-D-13-070.1

de Jong, M. F., & de Steur, L. (2016). Strong winter cooling over the Irminger Sea in winter 2014–2015, exceptional deep convection, and the emergence of anomalously low SST. *Geophysical Research Letters*, *43*, 7106–7113. https://doi.org/10.1002/2016GL069596

de Jong, M. F., Oltmanns, M., Karstensen, J., & de Steur, L. (2018). Deep convection in the Irminger Sea observed with a dense mooring array. *Oceanography*, *31*, 50–59. https://doi.org/10.5670/oceanog.2018.109

de Jong, M. F., van Aken, H. M., Våge, K., & Pickart, R. S. (2012). Convective mixing in the central Irminger Sea: 2002–2010. *Deep-Sea Research I*, *63*, 36–51. https://doi.org/10.1016/j.dsr.2012.01.003

Dickson, B., Yashayaev, I., Meincke, J., Turrell, B., Dye, S., & Holfort, J. (2002). Rapid freshening of the deep North Atlantic Ocean over the past four decades. *Nature*, *416*(6883), 832–837. https://doi.org/10.1038/416832a

Fan, X., Send, U., Testor, P., Karstensen, J., & Lherminier, P. (2013). Observations of Irminger Sea anticyclonic eddies. *Journal of Physical Oceanography*, *43*, 805–823. https://doi.org/10.1175/JPO-D-11-0155.1

Fratantoni, D. M. (2001). North Atlantic surface circulation during the 1990s observed with satellite-tracked drifters. *Journal of Geophysical Research*, *106*(C10), 22,067–22,093. https://doi.org/10.1029/2000JC000730

Fröb, F., Olsen, A., Våge, K., Moore, G. W. K., Yashayaev, I., Jeansson, E., & Rajasakaren, B. (2016). Irminger Sea deep convection injects oxygen and anthropogenic carbon to the ocean interior. *Nature Communications*, *7*, 13244. https://doi.org/10.1038/ncomms13244

García-Ibáñez, M. I., Pardo, P. C., Carracedo, L. I., Mercier, H., Lherminier, P., Ríos, A. F., & Perez, F. F. (2015). Structure, transports and transformations of the water masses in the Atlantic Subpolar Gyre. *Progress in Oceanography*, *135*, 18–36. https://doi.org/10.1016/j.pocean.2015.03.009

Holliday, N. P., Bacon, S., Cunningham, S., Gary, S. F., Karstensen, J., King, B. A., et al. (2018). Subpolar North Atlantic overturning and gyre-scale circulation in the summers of 2014 and 2016. *Journal of Geophysical Research: Oceans*, *123*, 4538–4559. https://doi.org/10.1029/2018JC013841

Holliday, N. P., Bersch, M., Berx, B., Chafik, L., Cunningham, S., Florindo-López, C., et al. (2020). Ocean circulation causes the largest freshening event for 120 years in eastern subpolar North Atlantic. *Nature Communications*, *11*, 585. https://doi.org/10.1038/s41467-020-14474-y

Josey, S. A., de Jong, M. F., Oltmanns, M., Moore, G. K., & Weller, R. A. (2019). Extreme variability in Irminger Sea winter heat loss revealed by Ocean Observatories Initiative mooring and the ERA5. *Reanalysis. Geophysical Research Letters*, *46*, 293–302. https://doi.org/10.1029/2018GL080956

Kanzow, T., & Zenk, W. (2014). Structure and transport of the Iceland Scotland overflow plume along the Reykjanes Ridge in the Iceland Basin. *Deep-Sea Research I*, *86*, 82–93. https://doi.org/10.1016/j.dsr.2013.11.003

Knutsen, Ø., Svendsen, H., Østerhus, S., Rossby, T., & Hansen, B. (2005). Direct measurements of the mean flow and eddy kinetic energy structure of the upper ocean circulation in the NE Atlantic. *Geophysical Research Letters*, *32*, L14604. https://doi.org/10.1029/2005GL023615

Krauss, W. (1995). Currents and mixing in the Irminger Sea and in the Iceland Basin. *Journal of Geophysical Research*, *100*(C6), 10,851–10,871. https://doi.org/10.1029/95JC00423

Lavender, K. L., Davis, R. E., & Owens, W. B. (2000). Mid-depth recirculation observed in the interior Labrador and Irminger Seas by direct velocity measurements. *Nature*, *407*(6800), 66–69. https://doi.org/10.1038/35024048

Li, F., Lozier, M. S., & Johns, W. E. (2017). Calculating the meridional volume, heat and freshwater transports from an observing system in the subpolar North Atlantic: Observing system simulation experiment. *Journal of Atmospheric and Oceanic Technology*, *34*, 1483–1500. https://doi.org/10.1175/JTECH-D-16-0247.1

Lozier, M. S., Bacon, S., Bower, A. S., Cunningham, S., de Jong, M. F., de Steur, L., et al. (2017). Overturning in the Subpolar North Atlantic Program: A new international ocean observing system. *Bulletin of the American Meteorological Society*, *98*, 737–752. https://doi.org/10.1175/BAMS-D-16-0057.1

Lozier, M. S., Li, F., Bacon, S., Bahr, F., Bower, A. S., Cunningham, S., et al. (2019). A sea change in our view of overturning in the Subpolar North Atlantic Program. *Science*, *363*(6426), 516–521. https://doi.org/10.1126/science.aau6592

Madec, G., & NEMO Ocean Engine. (2008). *Note du Pôle de modélisation, Institut Pierre-Simon Laplace (IPSL)* (No. 27). France.

Oltmanns, M., Straneo, F., & Tedesco, M. (2018). Increased Greenland melt triggered by large-scale, year-round cyclonic moisture intrusions. *The Cryosphere*, *13*, 815–825. https://doi.org/10.5194/tc-13-815-2019

Orvik, K. A., & Niiler, P. (2002). Major pathways of Atlantic water in the northern North Atlantic and Nordic Seas toward Artic. *Geophysical Research Letters*, *29*(19), 1896. https://doi.org/10.1029/2002GL015002

Petit, T., Mercier, H., & Thierry, V. (2018). First direct estimates of volume and water mass transports across the Reykjanes Ridge. *Journal of Geophysical Research: Oceans*, *123*, 6703–6719. https://doi.org/10.1029/2018JC013999

Petit, T., Mercier, H., & Thierry, V. (2019). New insight into the formation and evolution of the East Reykjanes Ridge Current and Irminger Current. *Journal of Geophysical Research: Oceans*, *124*, 9171–9189. https://doi.org/10.1029/2019JC015546

Piron, A., Thierry, V., Mercier, H., & Caniaux, G. (2015). Observations of basin scale deep convection in the Irminger Sea with Argo floats in the winter of 2011-2012. *Deep-Sea Research I*, *109*, 76–90. https://doi.org/10.1016/j.dsr.2015.12.012

Piron, A., Thierry, V., Mercier, H., & Caniaux, G. (2017). Gyre-scale deep convection in the subpolar North Atlantic Ocean during winter 2014–2015. *Geophysical Research Letters*, *44*, 1439–1447. https://doi.org/10.1002/2016GL071895

Racapé, V., Thierry, V., Mercier, H., & Cabanes, C. (2019). ISOW spreading and mixing as revealed by Deep-Argo floats launched in the Charlie-Gibbs fracture zone. *Journal of Geophysical Research: Oceans*, *124*, 6787–6808. https://doi.org/10.1029/2019JC015040

Reverdin, G., Niiler, P. P., & Valdimarsson, H. (2003). North Atlantic Ocean surface currents. *Journal of Geophysical Research*, *108*(C1), 3002. https://doi.org/10.1029/2001JC001020

Sarafanov, A., Falina, A., Mercier, H., Sokov, A., Lherminier, P., Gourcuff, C., et al. (2012). Mean full-depth summer circulation and transports at the northern periphery of the Atlantic Ocean in the 2000s. *Journal of Geophysical Research*, *117*, C01014. https://doi.org/10.1029/2011JC007572

Våge, K., Pickart, R. S., Sarafanov, A., Knutsen, Ø., Mercier, H., Lherminier, P., et al. (2011). The Irminger Gyre: Circulation, convection, and interannual variability. *Deep-Sea Research I*, *58*, 590–614. https://doi.org/10.1016/j.dsr.2011.03.001

van Aken, H. M., & Becker, G. (1996). Hydrography and through-flow in the north-eastern North Atlantic Ocean: The NANSEN project. *Progress in Oceanography*, *38*(4), 297–346. https://doi.org/10.1016/S0079-6611(97)00005-0

van Aken, H. M., & de Boer, C. J. (1995). On the synoptic hydrography of intermediate and deep water masses in the Iceland Basin. *Deep-Sea Research*, *42*, 165–189. https://doi.org/10.1016/0967-0637(94)00042-Q

van Aken, H. M., de Jong, M. F., & Yashayaev, I. (2011). Decadal and multi-decadal variability of Labrador Sea water in the north-western North Atlantic Ocean derived from tracer distributions: Heat budget, ventilation, and advection. *Deep-Sea Research I*, *58*, 505–523. https://doi.org/10.1016/j.dsr.2011.02.008

van Haren, H. (2007). Inertial and tidal shear variability above Reykjanes Ridge. *Deep-Sea Research I*, *54*, 856–870. https://doi.org/10.1016/j.dsr.2007.03.003

Volkov, D. (2004). Interannual variability of the altimetry-derived eddy field and surface circulation in the Extratropical North Atlantic Ocean in 1993–2001. *Journal of Physical Oceanography*, *35*, 405–426.

Yashayaev, I. (2007). Hydrographic changes in the Labrador Sea, 1960–2005. *Progress in Oceanography*, *73*(3–4), 242–276.

Zhang, Z., & Moore, J. C. (2015). Chapter 6—Empirical orthogonal functions. In Z. Zhang, & J. C. Moore (Eds.), *Mathematical and physical fundamentals of climate change* (pp. 161–197). Boston, MA: Elsevier. https://doi.org/10.1016/B978-0-12-800066-3.00006-1

Zou, S., Lozier, M. S., & Xu, X. (2020). Latitudinal structure of the meridional overturning circulation variability on interannual to decadal time scales in the North Atlantic Ocean. *Journal of Climate*, *33*(9), 3845–3862. https://doi.org/10.1175/JCLI-D-19-0215.1

Zou, S., Lozier, M. S., Zenk, W., Bower, A., & Johns, W. (2017). Observed and modeled pathways of the Iceland Scotland Overflow Water in the eastern North Atlantic. *Progress in Oceanography*, *159*, 211–222. https://doi.org/10.1016/j.pocean.2017.10.003